Title

Uncommon Behavior of Li Doping Suppresses Oxygen Redox in P2-Type Manganese-Rich Sodium Cathodes

Journal

Advanced Materials, 33(52)

ISSN

0935-9648

Authors

Xiao, Biwei

Liu, Xiang

Chen, Xi

et al.

Publication Date

2021-12-01

DOI

10.1002/adma.202107141

Uncommon Behavior of Li Doping Suppresses Oxygen Redox in P2-type Manganese-Rich Sodium Cathodes

Biwei Xiao[†1], Xiang Liu[†2], Xi Chen[3], Gi-Hyeok Lee[4,5], Miao Song[6], Xin Yang[1], Fred Omenya[1], David M. Reed[1], Vincent Sprenkle[1], Yang Ren[7], Cheng-Jun Sun[7], Wanli Yang[4], Khalil Amine[2,8], Xin Li[3], Guiliang Xu[2*], Xiaolin Li[1*]*

1. Energy & Environment Directorate, Pacific Northwest National Laboratory, Richland, WA, 99352, USA

2. Chemical Sciences and Engineering Division, Argonne National Laboratory, 9700 South Cass Avenue, Lemont, IL 60439, USA

3. John A. Paulson School of Engineering and Applied Sciences, Harvard University, Cambridge, MA 02138, USA

4. Advanced Light Source, Lawrence Berkeley National Laboratory, Berkeley, CA 94720, USA

5. Department of Materials Science and Engineering, Dongguk University, Seoul, Republic of Korea

6. Physical and Computational Sciences Directorate, Pacific Northwest National Laboratory, Richland, WA, 99352, USA

7. X-ray science division, Argonne National Laboratory, Lemont, IL 60439, USA

8. Materials Science and Engineering, Stanford University, Stanford, CA 94305, USA

† These authors contributed equally to the paper.

Correspondence should be addressed to: lixin@seas.harvard.edu; xug@anl.gov; xiaolin.li@pnnl.gov

Keywords: layered cathode • Li doping • oxygen redox reactivity • cationic reactivity

Abstract

Utilizing both cationic and anionic oxygen redox reactions is regarded as an important approach to exploit high-capacity layered cathode materials with earth abundant elements. It has been popular strategies to effectively elevate the oxygen redox activities by Li-doping to introduce unhybridized O *2p* orbitals in Na_xMnO_2-based chemistries or enabling high covalency transition metals in P2-$Na_{0.66}Mn_xTM_{1-x}O_2$ (TM = Fe, Cu, Ni) materials. Here, we investigated the effect of Li doping on regulating the oxygen redox activities P2-structured $Na_{0.66}Ni_{0.25}Mn_{0.75}O_2$ materials. Systematic X-ray characterizations and ab initio simulations have shown that the doped Li has uncommon behavior in modulating the density of states of

the neighboring Ni, Mn and O, leading to the suppression of the existing oxygen and Mn redox reactivities and the promotion of the Ni redox. The findings provide a complementary scenario to current oxygen redox mechanisms and shed lights on developing new routes for high-performance cathodes.

1. Introduction

Recent decades have witnessed a global endeavor on decarbonization and an exponential growth of demand on renewable energy. To transform these intermittent clean energy resources into reliable and dispatchable electricity, rechargeable batteries that have been utilized extensively in portable electronics and electric vehicles are also being exceled as a major energy storage approach for electric grids. While Li-ion battery (LIB) continues to dominate the market, there is also an urgent need to search for alternatives considering the increasing concern on the raw material/supply chain sustainability. Sodium-ion battery (SIB) is the natural next-in-line technology because it not only shares similar mechanism to LIBs and can be conveniently adapted to the current battery manufacturing systems, but also has the intrinsic advantage on material abundance and global distribution.[1-4]

Layered oxide cathode materials on the basis of intercalation chemistry have been extensively used in LIBs. Among them, manganese-rich materials with both the cationic and anionic oxygen redox reactions can deliver high electrochemical performance without using critical elements.[5, 6] The case can be replicated to the exploration of high performance SIB materials, where various materials with oxygen redox have been reported.[7-10]. Unlike the LIB materials with O3 structure, the SIB materials include both O3 and P2 structures (“P” and “O” stand for the Na-ion occupations on trigonal prismatic and octahedral sites, respectively).[7, 10] Conventional wisdom believed that extra Li doped in the transition metal (TM) layer of these materials triggers oxygen redox activities. The oxygen redox are related to the oxygen lone pair states in the A-O-A’ configuration, where A is one type of alkaline metal (Li or Na) and A’ is a specie in the TM layer hat does not hybridize with the oxygen *2p* orbital.[11, 12] Li-O-Li, Na-O-Na, Na-O-Li, Na-O-Mg, and Na-O-vacancy have been found responsible for the oxygen redox activity in O3 layered Li-rich materials, O3 layered Na-rich materials, Li- and/or Mg-doped P2 layered sodium materials and their vacancy-containing derivatives.[8, 11-16]

Recent extensive studies on sodium layered materials have brought up a new mechanism regarding the oxygen redox, as some materials that are not supposed to have the A-O-A’ local configuration also display oxygen redox activities. For example, P2-structured $Na_{2/3}Mn_{2/3}Ni_{1/3}O_2$ and its Fe and Cu-doped analogues have been observed to have such

activities with a long plateau at the high voltage region.[17-20] High covalency of the TMs at charged state leads to substantially increased oxygen density near the Fermi level, which triggers the oxygen redox.[13, 17, 21] The high voltage plateau in P2-structured $Na_xNi_yMn_{1-y}O_2$ historically have been ascribed to the P2-O2 phase transition and Li doping has been considered to diminish/eliminate the high voltage plateau and phase transition.[22-26] With the acknowledgement of oxygen redox existing in P2-structured $Na_xNi_yMn_{1-y}O_2$, it is now very intriguing to revisit the system and investigate the Li doping effect on the cationic and anionic redox reactions.

In this study, using P2-structured $Na_{0.66}Ni_{0.25}Mn_{0.75}O_2$ (NNMO) and the Li doped version of $Na_{0.66}[(Ni_{0.25}Mn_{0.75})_{0.9}Li_{0.1}]O_2$ (NLNMO) as the model material systems, we have elaborated the effect of Li doping on the redox activities of TM and oxygen using systematic X-ray characterization and functional theory (DFT) simulations. The substitution of 10% Li to the TM layer in NLNMO has demonstrated an effective suppression of the existing oxygen and Mn redox activities that occurred in the NNMO. Meanwhile the Li doping promotes the $Ni^{2.x+}/Ni^{4+}$ redox activity, leading to an elevated operating voltage of 0.2 V and hence 10% energy density increase. The effect is found to originate from the complicated interaction between Li and TM ions, which modulates the electronic structures of all the elements in the compound, resulting in an increase of Ni density of state (DOS) and decrease of the Mn and O ones near the Fermi level. The discovery of Li suppressing rather than promoting oxygen redox provides a complementary scenario to recent reductive coupling mechanism.[13, 17, 27] While the Li-doping is beneficial to the oxygen redox activity in Na_xMnO_2-based chemistries, it is quite different when Ni exists in the TM layers. The insight may also help reveal new routes for the development of high-performance Li and Na ion battery cathodes.

2. Results and discussions

The synthesized NNMO and NLNMO have similar spherical morphologies (Figure S1) with a diameter of ~ 20 μm and each sphere is constructed by nanoplate-shaped primary particles. Figures 1a-b show the powder X-ray diffraction (XRD) patterns of these materials and Rietveld refinement. Tables S1-2 are the summarized refinement results. Both materials display P2 layered structures with a space group of $P6_3/mmc$. This is corroborated by the atomic structures observed from the high-angle annular dark field scanning transmission electron microscopy (HAADF-STEM) and annular bright field (ABF)-STEM shown in the insets of Figures 1a-b. The interlayer spacings measured from the STEM images of the materials are ~5.5 Å, consistent with the refined XRD results. A pair of weak superstructure

diffraction peaks emerges at ~22⁰ (blue box and the enlarged box from 20-22.5°) in the XRD pattern of NLNMO. This is ascribed to the honeycomb cation ordering with Li in the TM layer.[10] However, this weak ordering disclosed by XRD cannot be observed in the HAADF and ABF-STEM images, as opposed to many other materials with Li in the TM layer. The absence of ordered Li-Mn structures from the microscopy images is most probably caused by the reduced domain size of the ordering region and the random presence of Ni in the structure. While the presence of superstructures has been found important in determining the hysteresis and reversibility of oxygen redox in Na_xMnO_2,[10] it may not be the sole prerequisite. As we will find out later, the NLNMO material with a superstructure actually has suppressed oxygen redox activity.

Figures 1c-d are the Mn and Ni *K* edge X-ray absorption near edge spectroscopy (XANES) results of NNMO and NLNMO. The Mn *K* edges both lie between Mn_2O_3 (Mn^{3+}) and MnO_2 (Mn^{4+}) standard spectra, yet the spectrum of NLNMO with Li substitution shows a shift to higher energy, suggesting higher Mn valence. The Ni K edges of both samples overlap well with each other, positioning slightly below $LiNiO_2$ (Ni^{3+}). Such observations indicate that the monovalent Li^+ substitution increases the valence of Mn for charge balance while the Ni valence is not affected. Figures 1e-f are the Fourier-transformed (ft) X-ray absorption spectroscopy (XAS) results showing the coordination environments of Mn and Ni in NNMO and NLNMO. In both figures, the peak at lower radial distance corresponds to the first shell TM-O coordination while the second coordination shell at higher radial distance relates to the TM-TM interaction. Figure 1e shows that the Li substitution did not induce any changes to the Mn-O coordination shell, however, the amplitude of the Mn-TM coordination shell has been obviously dampened, which is an indication that the incorporated Li largely reside in the TM layer. The occupation of lighter Li around Mn thus reduced the intensity of first shell Mn-TM scattering, corroborating the superstructure diffractions in the XRD patterns. However, the ft-Ni *K* edge XAS in Figure 1f did not show obvious dampening, suggesting that the incorporated Li-ions are mainly surrounded by Mn ions, which is consistent with the high Mn to Ni ratio in NLNMO and the nuclear magnetic resonance (NMR) reported previously.[26] The Li-doping shows different tuning effect on the local electronic structure of Mn and Ni, thus shapes the electrochemical behaviors of both elements, as well as the anion (*vide infra*).

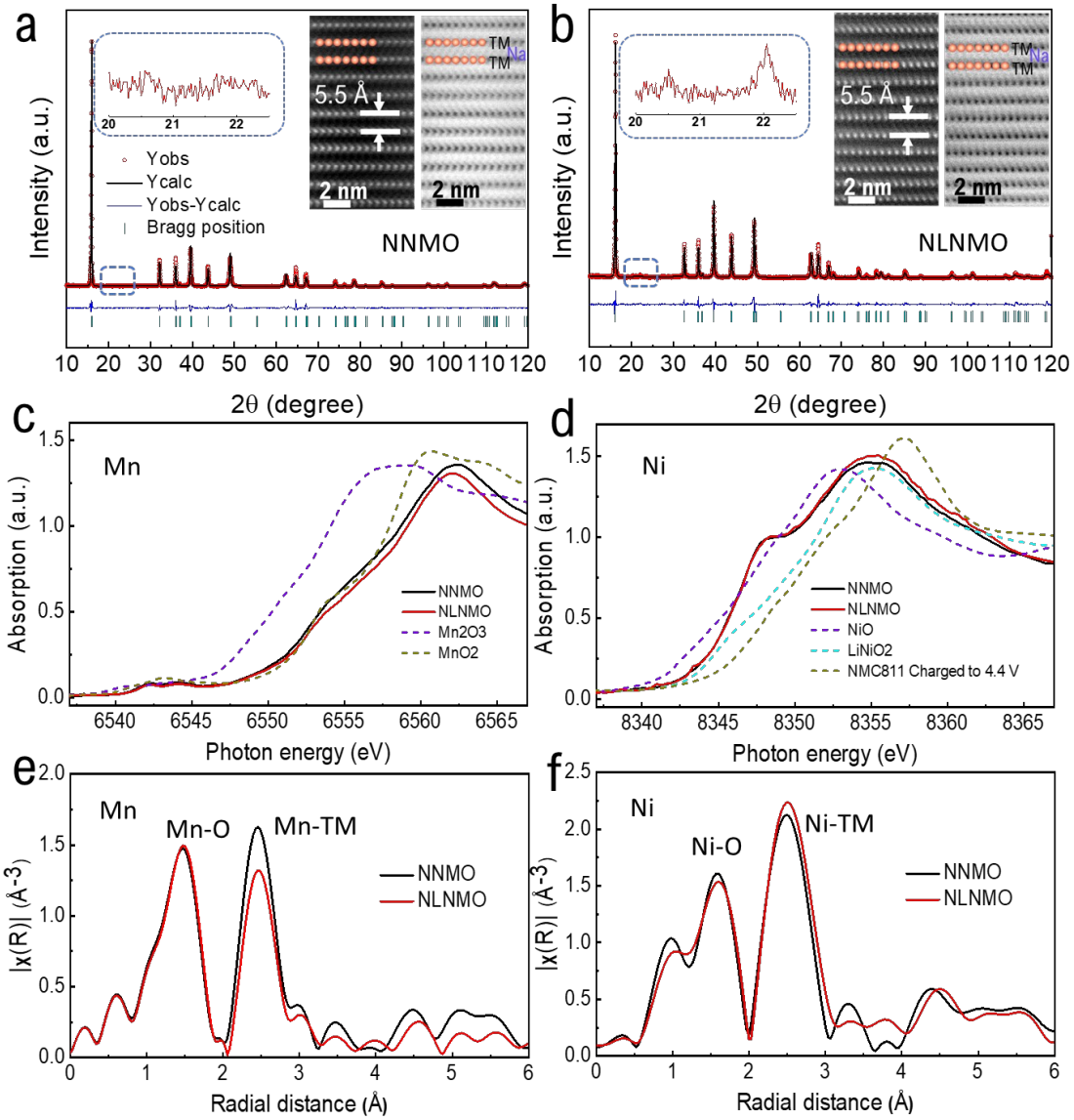

Figure 1. Characterization of the pristine NNMO and NLNMO materials. (a-b) Powder XRD patterns with Rietveld refinement (insets: HAADF and ABF-STEM images of NNMO and NLNMO, magnified super-structure diffraction region of NNMO and NLNMO). (c-d) Mn and Ni *K* edge XANES of NNMO and NLNMO. (e-f) Fourier-transformed Mn and Ni edge XAS of NNMO and NLNMO.

The electrochemical behaviors of NNMO and NLNMO were evaluated using localized high concentration electrolyte (LHCE).[28, 29] Figures 2a-b show the 1st charge/discharge curves and their corresponding dQ/dV curves of NNMO and NLNMO at 0.1C (1C=160 mA/g). NNMO shows a pair of plateaus above 4.2 V. Almost 40% of the charge capacity is from the charge plateau above 4.2V while the discharge capacity from that plateau is relatively low indicating a poor redox reversibility. It is also interesting to note that the discharge curve to 1.5V has over 1/3 capacity from the region below 2.2 V. NLNMO does not have the high

voltage plateau, and the discharge capacity below 2.2 V is substantially lower. The dQ/dV curves (Figure 2b) show that the NNMO displays three active regions at low, medium, and high voltage ranges (green, teal, and brown colored regions labeled with I, II and III), and most of the capacity is derived from the low and high ranges. In comparison, the NLNMO shows a much more concentrated capacity originated from the medium voltage range, and the high voltage plateau has been largely suppressed. Figures 2c-d show the charge/discharge curves and corresponding dQ/dV curves of NNMO and NLNMO after 25 cycles. NNMO loses most of its high voltage redox activities. While the charge/discharge curves of NNMO and NLNMO show similar capacity, the NLNMO shows greatly elevated voltage between 1.5 and 3 V.

Figure 2e-f shows the comparison of the cycling performances and average discharge voltages of NNMO and NLNMO. NNMO shows slightly higher capacity than NLNMO yet it decays fast in the initial few cycles due to the presence of the high voltage plateau. From about the 10^{th} to the 100^{th} cycle, NNMO and NLNMO display stable performance with similar capacity. The NLNMO shows a large boost of average discharge voltage over the long-term cycling. As shown in Figure 2f, except for the first activation cycle where the average voltages in both materials appear to be very close because of the high voltage plateau in NNMO, the NLNMO sample demonstrates higher average voltage than NNMO. At stable cycling, the average discharge voltage of NLNMO is approximately 10% higher than NNMO, reaching ~ 3.25 V. The elevation of average voltage leads to an improvement of energy density from 407 Wh/kg to 440 Wh/kg and round-trip efficiency from 83% to 90% despite having the same capacity as summarized in Figure S2. The same trend is also observed in the tests under 1C in LHCE, and 0.5C in PC-based electrolyte (Figure S3), indicating that it is independent from the rate and electrolyte. Study of the NLNMO with 5% substitution (Figure S4 and Table S3) further verifies the Li doping effect. The electrochemical performance (e.g. charge-discharge curve and average voltage) shows mixed features of NNMO and NLNMO with 10% Li doping.

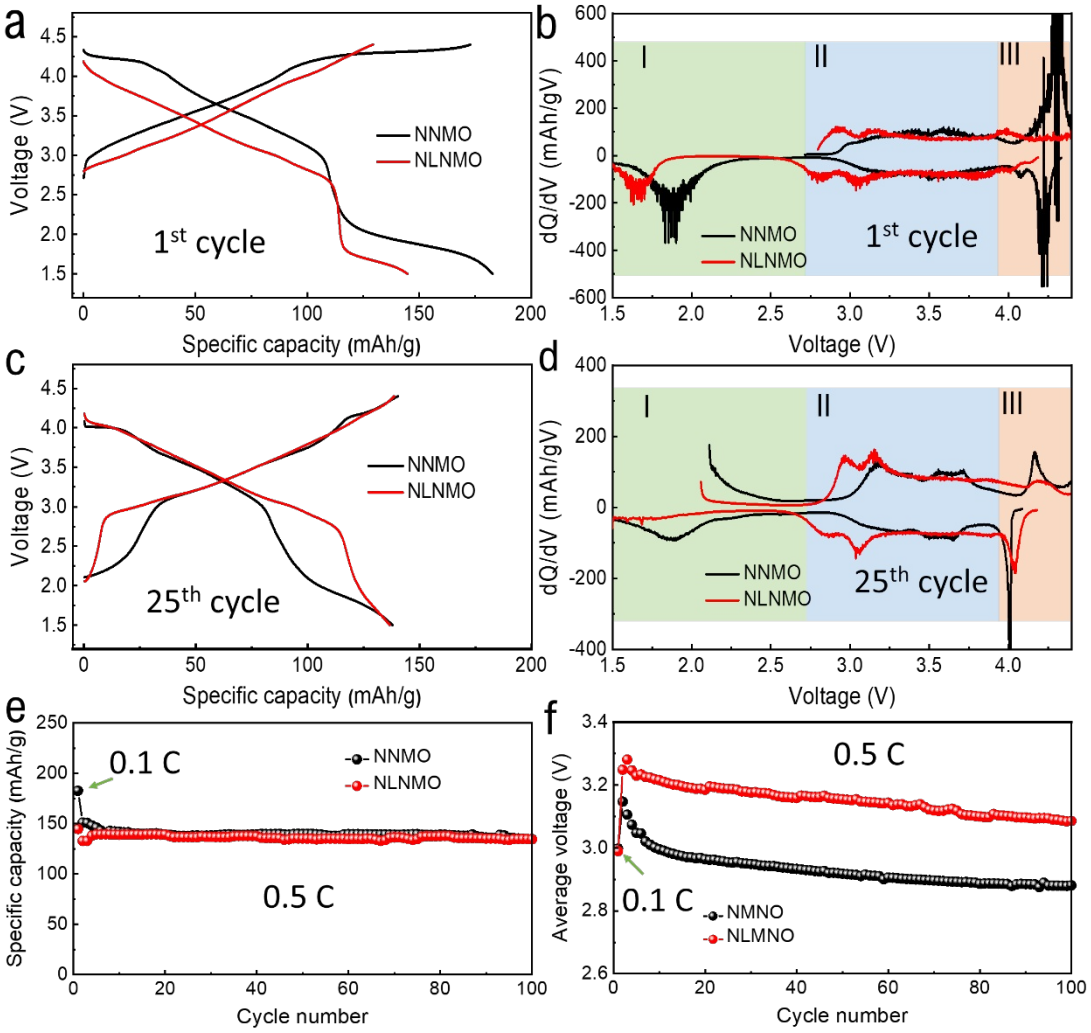

Figure 2. Electrochemical performance of NNMO and NLNMO. (a) Charge/discharge curves of the 1st cycle. (b) dQ/dV curves of the 1st cycle. (c) Charge/discharge curves of the 25th cycle. (d) dQ/dV curves of the 25th cycle. (e) Cycling performance at 0.5C with initial activation cycle at 0.1C. (1C = 160 mA/g) (f) Plots of the average discharge voltage along cycling.

To discuss the electrochemical activities of the oxygen, we have employed the high-efficiency mapping of the resonant inelastic X-ray scattering (mRIXS) at the O *K-edge*, which could distinguish the latticed oxidized oxygen signals from the strong TM-O hybridization entangled in the pre-edge features in conventional XAS experiments.[30-34] The mRIXS characterization has been demonstrated to be a powerful technique for detecting the lattice oxidized oxygen states in charged SIB electrodes,[4, 19] which have strong and broad TM-O hybridization feature and oxidized oxygen feature distinguished at the fingerprinting energies around 524 eV emission and 531 eV excitation, consistent with the O-*K* mRIXS features of standard oxidized oxygen references such as peroxide and O_2.[35, 36] Figures 3a and 3b display

the O-*K* mRIXS results of NNMO and NLNMO at 4.4V after the 1st charge. Besides the typical broad TM-O hybridization features around 525 eV emission energy in both maps, the charged NNMO electrode displays a finite amount of intensity at the fingerprinting energies of oxidized oxygen (red circle in Figure 3a). In contrast, no intensity of oxidized oxygen could be detected for NLNMO (red circle in Figure 3b). Such a contrast could be better illustrated by integrating the mRIXS intensity into the RIXS cuts and the mRIXS super-partial fluorescence yield (sPFY) spectra, as shown in Figures S5 and could be consistently observed through the 2nd cycle charged electrodes (Figures S6).

It is important to note that, although many oxygen redox compounds display the high-voltage plateau associated with the oxygen redox reactions, the plateau itself should not be simply taken as a signature of oxygen redox reactions as they could be just from oxygen release and strong surface reactions.[37] Therefore, such a reliable spectroscopic characterization of mRIXS is critical. Additionally, it has been found that the thermal stability also can be associated with the oxygen electrochemical activities.[38] Oxygen redox can lead to destabilized lattice oxygen, which may release in the form of oxygen upon heating. Figure S7a shows the mass spectrometry results on the oxygen release from thermal treatments of charged NNMO and NLNMO samples. NNMO exhibits a strong oxygen release peak at ~290 ^{o}C, which is greatly suppressed in NLNMO. The CO_2 release (Figure S7b) at the same temperature range is also suppressed in NLNMO following the low O_2 release. Our spectroscopic and thermal stability tests consistently suggest that Li substitution suppressed the oxygen redox activities in the NNMO system when charged to high voltages.

The mechanism of the oxygen redox in the NNMO material and its suppression in NLNMO is intriguing. O *2p* orbital holes usually are critical to activate the anion redox of Na_xMnO_2-based chemistries and hence Li, Mg, and vacancy have been introduced to enhance non-hybridized oxygen.[8-10, 13, 27, 39] In the cases where there is no unhybridized oxygen *2p* orbitals created, oxygen *2p* orbital holes are formed by leveraging the reductive coupling mechanism, for instance, hybridizing the oxygen with highly electronegative cations like Ni^{4+}. The electrons in the O *2p* orbital can jump to the Ni *3d* orbitals, leaving holes in the O *2p* orbital.[12, 21] The oxygen redox in the NNMO analogous materials is a result of this mechanism.[20] However, the fact that NLNMO with unhybridized O 2p orbital through Li-O-Na configuration display a suppressed oxygen redox implies that the interaction of Li with the various TMs plays a crucial role.

In-situ XRD and ex-situ XAS have been carried out to investigate the different phase transitions and binding environment evolutions of the TMs in NNMO and NLNMO. Side-by-side comparison of the in-situ XRD results (Figures S8-S9) shows that NNMO has additional (002) peak broadening and intensity drop at the end of charge while NLNMO mainly exhibits the peak shifting to low degree. Another significant difference is that the shift of the NLNMO (100) and (102) peaks to low angle during charge is more significant than that of NNMO while it is the opposite for the reverse shift during discharge. The shift of NNMO (100) and (102) peaks to high angle during discharge continues to below 2.0V, leading to a more severe P2 to P2' transition and a significantly long tail plateau at the end of discharge curve. These results suggest higher degree of TM oxidization in NLNMO during charge while higher degree of reduction in NNMO during discharge.

To further specify the change of the TMs valence, Mn and Ni K edge XAS of NNMO and NLNMO at different state of charges (SOCs) have been systematically investigated. Figures 3c-f are the ex-situ XANES results. In NNMO (Figure 3c), the Ni valence at pristine state locates between NiO and $LiNiO_2$ (solid black, dash purple and teal traces), indicating a valence between 2+ to 3+. When charged to 4.4 V, the Ni is oxidized to a position between $LiNiO_2$ (Ni^{3+}) and charged $LiNi_{0.8}Mn_{0.1}Co_{0.1}O_2$ (NMC811, Ni^{4+}) (solid red, dash teal and brown traces) as can be told from the positive shift of the edge jump. Upon discharging to 3.0 V, the Ni is reduced to the original state, further discharging to 1.5 V does not generate any more changes (solid green and blue traces). The result indicates that the long tail plateau at the end of discharge is not caused by the reduction of Ni. In NLNMO (Figure 3d), however, different degree of Ni redox participation is observed. While the Ni in the pristine NNMO and NLNMO appear to be at the same valence between 2+ and 3+ (solid black, dash purple and teal traces), the charging process involves different Ni oxidation. When charged to 4.4 V, NLNMO shows higher edge jump position compared to NNMO, which almost overlaps with that of the charged NMC811 (solid red and dash brown traces), demonstrating a final valence of 4+. When discharged to 3.0 V, the position is higher than the pristine NLNMO, the difference disappears when further discharged to 1.5 V (solid blue trace).

Determining subtle valence changes in Mn is rather tricky due to the involvement of multiple scattering processes.[38] In NNMO (Figure 3e), charging from pristine state (solid black trace) to 4.4 V (solid red trace) triggered slight edge shift to higher energy position, as well as absorption shape change. This indicates that the contribution from Mn during the charging process is limited. After discharging to 3.0 V (solid green curve), the edge position

and line shape return to the pristine state. Further discharging to 1.5 V (solid blue curve) leads to a major shift of edge position to a lower valence between MnO_2 (Mn^{4+}, dash brown trace) and Mn_2O_3 (Mn^{3+}, dash purple trace). Such observation indicates that the long tail plateau at 1.5-3.0 V in NNMO during discharging originated from the reduction of Mn. In NLNMO (Figure 3f), charging from pristine state (solid black trace) to 4.4 V (solid red trace) did not cause any edge jump or position shift, implying the absence of Mn oxidation during charging. After discharging to 3 V (solid green trace) did not involve any energy shift either. Only further discharging to 1.5 V (solid blue trace) leads to slight Mn reduction, despite far less intensive compared to NNMO at the same SOC (dashed blue trace).

The above XANES results suggest that both Ni and Mn contribute to the redox activity in NNMO. Ni is active at medium to high voltage regions while Mn is active at low voltage region. In the case of NLNMO, Mn becomes largely suppressed, and Ni serves and the major redox center, and it is more active than the Ni in NNMO. The Mn *K* edge data of these two samples provide more information than just valences. The pre-edges of Mn *K* edge XAS corresponds to the transition from its *1s* to the *3d* orbitals that are largely hybridized with the O *2p* orbitals, thus providing abundant information to the local hybridization structures.[40] In most of the in-situ XAS studies, the Mn pre-edge intensity increases along with the charging process due to the gradually distorted MnO_6 octahedra.[38, 40] In NNMO (Figure 3e, inset), the pre-edge peak of the sample charged to 4.4 V (solid red trace) shows less intensity than that of the pristine state (solid black trace), contradicting to conventional findings. Such abnormal observation further corroborates the participation of oxygen in the redox process, which results in the creation of local oxygen vacancies. The lack of Mn-O hybridization leads to a drop of pre-edge intensity. The NLNMO sample did not show such change (Figure 4d, inset), corroborating the suppression of oxygen redox.

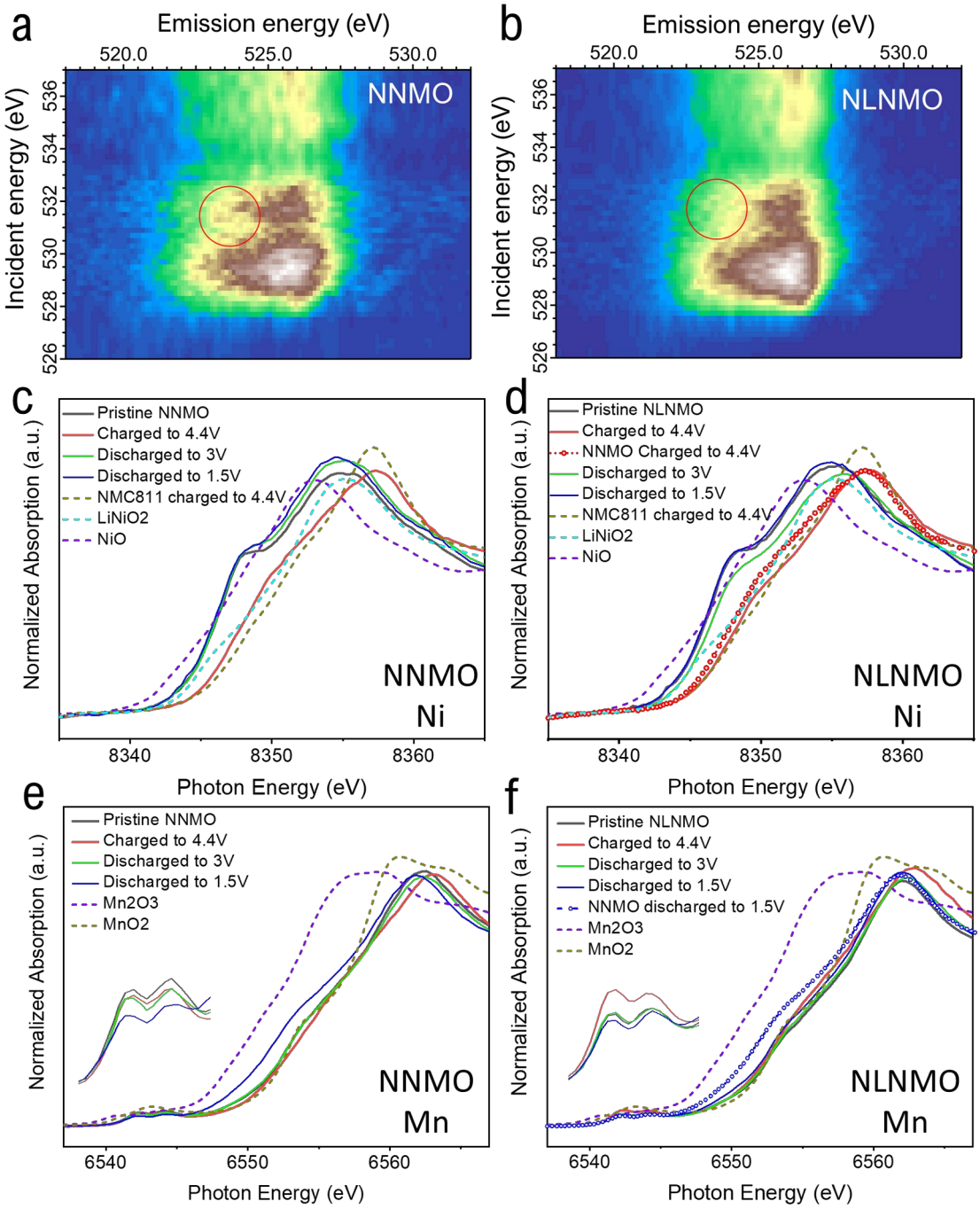

Figure 3. mRIXS and XAS characterization of the redox activities of oxygen and TM. (a-b) O *K-edge* mRIXS results of NNMO and NLNMO at the 1st 4.4 V charged states. ex-situ XANES of (c) Ni *K-edge* of NNMO. (d) Ni *K-edge* of NLNMO. (e) Mn *K-edge* of NNMO. (f) Mn *K-edge* of NLNMO (inset figures in e and f: magnified pre-edges).

It is known that the oxidation activities of the TM and oxygen upon charging relies on the relative energy of the TM against oxygen states.[11] DFT calculation of the DOS for the fully sodiated and charged NNMO and NLNMO materials have been carried out to investigate the local electronic structure evolution of Ni, Mn and O with and without the Li

substitution. The supercell was constructed based on the formula of $Na_xMn_{3/4}Ni_{1/4}O_2$ (Figure S11), with 12 TM ions (9 Mn and 3 Ni) per layer (labelled as NNMO in Figure 4). The number of x corresponds to the materials at different states of charge. Doping Li creates 1/12 Li composition in the TM layer, and we tried several typical scenarios of Li doping environment and found some unique electronic behaviors that can well match the above experiments from the supercell with the doped Li surrounded by 4 Mn and 2 Ni ions as immediate neighboring ions (labelled as NLNMO in Figure 4), while other local Li environments cannot match well, such as 5 Mn and 1 Ni ions.

As shown in Figure 4a-b, at fully sodiated state (Na1), both NNMO and NLNMO show some Mn and O DOS just below the Fermi level, projected from the top two occupied energy bands. When the Na composition is 2/3 (Na2/3), i.e., at the directly synthesized or low charge state, compared with the undoped case (Figure 4c), the Li doped supercell shows a significant DOS increase projected from those two bands that are mainly contributed by the Ni ions around the doped Li (Figure 4d). At the low Na composition of 1/6 or a high charge state (Na1/6), the DOS near Fermi level in NLNMO, compared with the NNMO (Figure 4e), is further contributed by the Ni ion that does not surround the Li (Figure 4f).

Quantitatively, the integrated DOS area of the top two bands below the Fermi level was leveraged to estimate its contribution to the redox activity.[17] Figures 4g-h show the integrated partial DOS intensity for each type of the ions in NNMO (Fig. 4g), and in NLNMO (Fig. 4h), respectively. We observe a clearly increased DOS of O upon desodiation in NNMO without Li doping, where the DOS intensities near Fermi level for the fully charged state of Na1/6 is increased by around 40% compared with Na2/3. While for fully charged NLNMO with Li doping at Na1/6, this change of O DOS is not observed. This suggests a more active oxygen redox activity in NNMO at high voltage state, consistent with our experimental results on the suppressed oxygen redox by Li doping at high voltage (Figure 2 and Figure 3).

Similarly, the DOS trend of TMs in Figure 4g suggests that Mn is the main redox center at low voltages from Na1 to Na2/3, while there is a switch to Ni as the main redox center at high voltages from Na2/3 toward Na1/6 for NNMO, indicated by a suppression of Mn DOS intensity and a significant increase of Ni DOS. For NLNMO with Li doping, however, the switch to Ni redox accompanied by the Mn redox suppression seems to happen at a much lower voltage range from Na1 to Na2/3 (Figure 4h), as indicated by the already high Ni DOS intensity at Na2/3. From Figure 4h, we also notice that from Na2/3 toward Na1/6, there is likely a switch of Ni redox contribution from those Ni ions neighboring the

doped Li ion to those away from it. The computational results here are consistent with the experimental results of NLNMO showing higher average voltage of ~0.3 V in the low voltage range below 2.2 V (Figure 2), as Ni redox voltage is higher than the Mn redox. The result is also consistent with the XAS results in Figure 3.

The fact that the oxygen redox is suppressed with significantly more formation of Ni^{4+} at a fully charged state with Li doping is very intriguing. The results provide complementary supports to the recent mechanism of high covalency of the TMs leading to the substantial increases the oxygen density near the Fermi level and triggering the oxygen redox of P2-structured $Na_{2/3}Mn_{2/3}Ni_{1/3}O_2$.[13, 21] It also suggests that it is not universally applicable to use Li for the activation of oxygen redox. In Na_xMnO_2-based compositions, Li-doping can substantially increase the oxygen redox. However, when there is Ni in the TM layer, the doped Li may change the local electronic structures and suppress the oxygen redox by promoting the Ni ones instead.

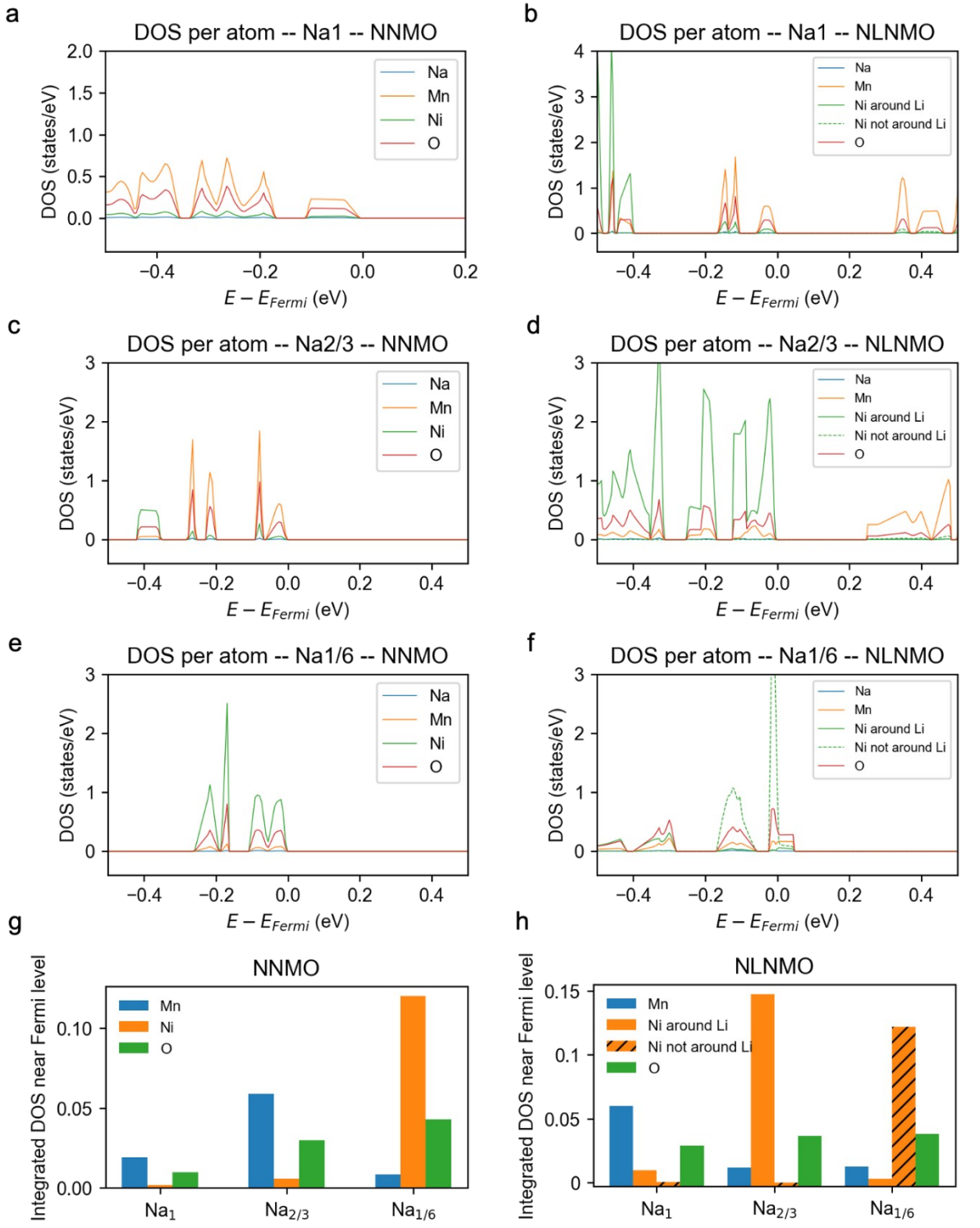

Figure 4. (a-f). DFT calculated partial density of state (DOS) for different elements of Na, Mn, Ni, O at different Na compositions of 1.0 (a, b), 2/3 (c, d) and 1/6 (e, f) for NNMO without Li doping (a, c, e) and NLNMO with Li doping (b, d, f). g-h. Integrated DOS projected from the top two bands below Fermi level for Mn, Ni and O ions in (g) pristine and (h) NLNMO. In each case, the integrated DOS is normalized such that the sum of contributions from Mn, Ni and O is one, to highlight their relative contributions. For NLNMO

with Li doping, the Ni ions are further classified depending on if they are neighboring the doped Li or not.

3. Conclusions

We have synthesized P2-structured $Na_{0.66}Ni_{0.25}Mn_{0.75}O_2$ (NNMO) material with and without Li doping. By using them as model materials, we have demonstrated the effect of Li doping on the redox activities of TM and oxygen ions. RIXS, XAS, MS, in-situ XRD experiments and DFT simulations have been systematically carried out side-by-side. While previous studies on the Li doped P2-structured $Na_xLi_zNi_yMn_{1-y-z}O_2$ historically have ascribed the performance improvements versus undoped materials mainly to the inhibition of the P2-O2 phase transition, our work has elucidated an important additional role of Li doping on the redox engineering. First, we have furthered the understanding on the correlation of oxygen redox activity and unhybridized O *2p* orbital. The introduction of unhybridized Li-O bonds to trigger oxygen redox works for Na_xMnO_2-based materials, yet it is not a universal case. With Ni in the TM layer, Li substitution modifies the cation redox reaction and suppresses the already existing oxygen redox instead. Second, we have provided a complementary scenario to the finding on the reductive coupling mechanism on oxygen redox activity. P2-structured $Na_{2/3}Mn_{2/3}Ni_{1/3}O_2$ and its Fe and Cu-doped analogues have the oxygen redox activity enabled by high covalency of the TMs at charged state. However, the fact that NLNMO with more Ni^{4+} formation displays suppressed oxygen redox implies that the detail interaction of Li with the TMs is complicated and plays a crucial role here. Further analysis of the fundamental driving force and the correlation of oxygen redox reactivity with the TM-O hybridization is needed. At last, we have demonstrated good electrochemical performances for the 10% Li doped cathode material. Although the suppressed oxygen and Mn redox activities by Li doping likely lead to reduced capacities at the initial few cycles, the capacity approach the same level quickly for both Li doped and undoped cases. Li doping, however, significantly enhanced Ni redox activity in the low voltage range and elevated the operating voltage and energy density. It also has improved thermal stability with much less O_2 releases upon heating. This is a critical factor that needs to be considered in future works involving the attempt of utilizing the oxygen redox activity. The understanding revealed in our work provides a guidance for the development of future high-performance alkaline-ion battery cathodes.

4. Experimental Section

Material synthesis: The precursor of $Mn_{0.75}Ni_{0.25}CO_3$ spheres were synthesized through a carbonate co-precipitation approach. Typically, stoichiometric amount of $MnSO_4 \cdot 6H_2O$ (Sigma Aldrich, 99%) and $NiSO_4 \cdot H_2O$ (Sigma Aldrich, 99%) (molar ratio = 3:1) were dissolved in de-ionized water with a total concentration of 2M (Solution A). 2.3 M Na_2CO_3 aqueous solution was used as the precipitant (Solution B). Afterwards, Solution B was pumped into Solution A placed in the continuous stirred tank reactor (CSTR, Eppendorf) with controlled PH and simultaneous N_2 feeding. The resulted powder was collected, fully washed with DI water, and dried at 120 ^oC under vacuum.

To synthesize P2 NNMO and NLNMO cathodes, desired amount of the above carbonate precursors were mixed with NaOH (Sigma Aldrich, 99%) and LiOH (Sigma Aldrich, 99%) at desired ratios, pressed into pellets and calcined at 700 ^oC for 14h in O_2 atmosphere. The samples were then collected, ground, and stored in the glovebox for future use.

Non-spherical NNMO was synthesized through a solid-state synthesis approach. Stoichiometric amount of Na_2CO_3, NiO, and Mn_2O_3 (Sigma Aldrich, 99%) was ball-milled for 12h at 450 rpm, pressed into pellet and fired at 900 ^oC for 14 h in O_2 atmosphere.

Material characterization

X-ray diffraction (XRD): The powder XRD patterns were collected using a Rigaku Miniflex II XRD at a scan rate of 0.2^o/min from 10 to 120^o. To avoid unnecessary exposure to air, all the powder samples were covered by Kapton film during measurement.

In-situ synchrotron XRD: In situ high-energy XRD of the cathodes during charge/discharge were measured at Beamline 11-ID-C of Advanced Photon Source at Argonne National Laboratory. The wavelength is 0.1173 Å. Coin cells with holes for beam pass were used to make the in-situ cell. The holes at the top and bottom cases of the coin-cell were sealed with Kapton tape after cell assembly. The electrode had a mass loading of ~5 mg/cm^2. the in-situ cell was rested for 5 h before doing in-situ XRD. During the in-situ experiment, an MACCOR cycler was used to discharge/charge the cell using a constant rate of 12 mA/g between 1.5 and 4.4 V.

Mapping of the resonant inelastic X-ray scattering (mRIXS): The RIXS spectra were measured by the iRIXS endstation at Beamline 8.0.1 of Advanced Light Source, Lawrence Berkeley National Laboratory.[41] The spectra were collected through an ultra-high efficiency modular spectrometer, the energy resolutions of emission energy and incident energy are 0.25 and 0.35 eV, respectively. Based on the collected RIXS spectra, the 2D mRIXS spectra were

organized by the multi-step data processing including normalization to beam flux and collecting time, etc. The intensity of the mRIXS is represented at color scale. For the further clarification of the oxygen redox feature in mRIXS spectra, the integrated RIXS cuts and mRIXS-super partial fluorescence yield (mRIXS-sPFY) spectra were generated based on the mRIXS spectra. The integrated RIXS cuts were made of the RIXS cuts collected by incident energies from 530.7 to 531.7 eV. The mRIXS-sPFY spectra were generated by integrating the mRIXS intensity between the emission energies from 522.5 to 524.5 eV.

Heating with mass spectrometry (MS): The charged NNMO and NLNMO cathode powder was collected from coin cells after the 1st charge. The coin cells were disassembled in the glove box and loaded into a quartz capillary tube with a controllable heating unit. Ultra-high-purity argon was used as the carrier gas and a residual gas analyzer was utilized to measure the outgassing of the cathode during heating. The heating rate was 10^{o}C/min from room temperature to 600^{o}C.

XANES and EXAFS characterizations: The X-ray near edge spectroscopy (XANES) reveals the information on the oxidation state and coordination geometry of the absorbing atom, while the extended X-ray absorption fine structure spectroscopy (EXAFS) tells the local structure of the absorbing atom. The ex-situ XAS characterization was utilized at Beamline 20-BM at APS of Argonne National Laboratory. The Ni, Co and Mn K-edges were collected at the transparent mode. The EXAFS data were extracted and normalized with established methods using the ATHENA software package, and the EXAFS data in the region of 0-6 Å were displayed.

SEM and HAADF-STEM: SEM images were acquired using Helios NanoLab 600i (Thermo Fisher Scientific, USA) operated at 2–30 kV. An aberration-corrected TEM (Titan from Fisher Thermal, USA) equipped with a high-angle annular dark-field (HAADF) detector was employed at 300 kV for HAADF scanning TEM (STEM.

Computation: All DFT calculations were carried out by the Vienna Ab initio Simulation Package (VASP), which implements the pseudopotential plane-wave band method.[42] The projector augmented wave Perdew–Burke–Ernzerhof (PAW-PBE) functional was utilized for the exchange-correlation energy. A 520-eV plane-wave energy cutoff was implemented for all calculations. The generalized gradient approximation[43] (GGA)+U scheme of the Perdew-Burke-Ernzerhof (PBE) functional was used, with U = 3.9 eV and 6.0 eV for Mn and Ni, respectively.[44] All computations were performed in 3x4x2 sized P2 stacking of supercells, with 12 transition metal ions in each layer and 2 transition metal layers.

The energy converges to 10^{-5} eV for electronic iteration and the residue forces converge to 0.1 eV/A for ionic relaxation. The Monkhorst package for k-point mesh is used with k-points separation of fewer than 0.04 A^{-1}. The energy converges to 10^{-6} eV for electronic iteration in the density of state calculation.

Electrochemical measurement: The electrodes were made by mixing the active material, super P carbon and polyvinylidene fluoride (PVDF) with a ratio of 80:10:10 dispersed in N-methyl-2-pyrrolidone (99%, Alfa Aesar) using a Thinky ARE350 mixer. The slurry was pasted onto Al foil and dried under 120 ^{o}C in a vacuum oven overnight. The active material loading was controlled to be around 5 mg/cm^2. The electrodes were thereafter punched and assembled in CR2032 coin cells in a glovebox filled with argon gas. The O_2 and H_2O levels are below 1 ppm. Na metal (99.5%, Alfa Aesar) was used as the counter electrode. For the cells tested in localized high concentration electrolyte (LHCE), the electrolyte is composed of 5.2M NaFSI (Oakwood Chemicals) dissolved in dimethoxyethane (Gotion Inc.) diluted by bis(2,2,2-trifluoroethyl) ether (BTFE). For the cells tested in carbonate electrolyte, the electrolyte is composed of 1M $NaPF_6$ dissolved in ethyl carbonate (EC)/ propylene carbonate (PC) (1:1 vol%). The coin cells were tested using an Arbin Battery Tester between 1.5-4.4V at desired rates in room temperature.

Supporting Information

Supporting Information is available from the Wiley Online Library or from the author.

Acknowledgments

Biwei Xiao and Xiaolin Li et. al. would like to thank the support from the U.S Department of Energy (DOE) Office of Electricity (Contract No. 70247A). Pacific Northwest National Laboratory is a multiprogram laboratory operated by Battelle Memorial Institute for the DOE under Contract DE-AC05-76RL01830. Research at the Argonne National Laboratory was funded by the US Department of Energy (DOE), Vehicle Technologies Office. Support from T. Duong of the US DOE's Office of Vehicle Technologies Program is gratefully acknowledged. Use of the Advanced Photon Source, an Office of Science User Facility operated for the DOE Office of Science by Argonne National Laboratory, was supported by DOE under contract no. DE-AC02-06CH11357. Xi Chen and Xin Li are supported by Data Science Initiative Competitive Research Fund and Climate Change Solutions Fund at Harvard. Computations were supported by the Extreme Science and Engineering Discovery Environment (XSEDE) and the Odyssey cluster of the FAS Division of Science Research Computing Group at Harvard University. Soft X-ray experiments were

performed at BL8.0.1 of the Advanced Light Source (ALS), a DOE Office of Science User Facility, under contract no. DE-AC02-05CH11231. G.-H.L. acknowledge the financial support of the ALS fellowship program.

B. Xiao and X. Liu contributed equally to this work.

Received: ((will be filled in by the editorial staff))
Revised: ((will be filled in by the editorial staff))
Published online: ((will be filled in by the editorial staff))

References

[1] D. Saurel, B. Orayech, B. W. Xiao, D. Carriazo, X. L. Li, T. Rojo, *Adv. Energy Mater.* **2018**, 8, 1703268.

[2] J. H. Song, B. W. Xiao, Y. H. Lin, K. Xu, X. L. Li, *Adv. Energy Mater.* **2018**, 8, 1703082.

[3] D. Kundu, E. Talaie, V. Duffort, L. F. Nazar, *Angew. Chem. Int. Ed.* **2015**, 54, 3431.

[4] J. Wu, Z. Zhuo, X. Rong, K. Dai, Z. Lebens-Higgins, S. Sallis, F. Pan, L. F. J. Piper, G. Liu, Y. D. Chuang, Z. Hussain, Q. Li, R. Zeng, Z. X. Shen, W. Yang, *Sci. Adv.* **2020**, 6, eaaw3871.

[5] B. W. Xiao, X. L. Sun, *Adv. Energy Mater.* **2018**, 8, 1802057.

[6] B. Xiao, Y. Wang, S. Tan, M. Song, X. Li, Y. Zhang, F. Lin, K. S. Han, F. Omenya, K. Amine, X. Q. Yang, D. Reed, Y. Hu, G. L. Xu, E. Hu, X. Li, X. Li, *Angew. Chem. Int. Ed.* **2021**, 60, 8258.

[7] Q. Wang, S. Mariyappan, G. Rousse, A. V. Morozov, B. Porcheron, R. Dedryvere, J. Wu, W. Yang, L. Zhang, M. Chakir, M. Avdeev, M. Deschamps, Y. S. Yu, J. Cabana, M. L. Doublet, A. M. Abakumov, J. M. Tarascon, *Nat. Mater.* **2021**, 20, 353.

[8] M. Ben Yahia, J. Vergnet, M. Saubanere, M. L. Doublet, *Nat. Mater.* **2019**, 18, 496.

[9] K. Du, J. Y. Zhu, G. R. Hu, H. C. Gao, Y. T. Li, J. B. Goodenough, *Energy Environ. Sci.* **2016**, 9, 2575.

[10] R. A. House, U. Maitra, M. A. Perez-Osorio, J. G. Lozano, L. Jin, J. W. Somerville, L. C. Duda, A. Nag, A. Walters, K. J. Zhou, M. R. Roberts, P. G. Bruce, *Nature* **2020**, 577, 502.

[11] D. H. Seo, J. Lee, A. Urban, R. Malik, S. Kang, G. Ceder, *Nat. Chem.* **2016**, 8, 692.

[12] H. Xu, S. H. Guo, H. S. Zhou, *J. Mater. Chem. A* **2019**, 7, 23662.

[13] G. H. Lee, V. W. H. Lau, W. L. Yang, Y. M. Kang, *Adv. Energy Mater.* **2021**, 2003227.

[14] C. Ma, J. Alvarado, J. Xu, R. J. Clement, M. Kodur, W. Tong, C. P. Grey, Y. S. Meng, *J. Am. Chem. Soc.* **2017**, 139, 4835.

[15] B. Mortemard de Boisse, G. Liu, J. Ma, S. I. Nishimura, S. C. Chung, H. Kiuchi, Y. Harada, J. Kikkawa, Y. Kobayashi, M. Okubo, A. Yamada, *Nat. Commun.* **2016**, 7, 11397.

[16] E. J. Kim, K. Mofredj, D. M. Pickup, A. V. Chadwick, J. T. S. Irvine, A. R. Armstrong, *J. Power Sources* **2021**, 481, 229010.

[17] I. Abate, S. Y. Kim, C. D. Pemmaraju, M. F. Toney, W. Yang, T. P. Devereaux, W. C. Chueh, L. F. Nazar, *Angew. Chem. Int. Ed.* **2021**, 60, 10880.

[18] C. Cheng, S. Li, T. Liu, Y. Xia, L. Y. Chang, Y. Yan, M. Ding, Y. Hu, J. Wu, J. Guo, L. Zhang, *ACS Appl. Mater. Interfaces* **2019**, 11, 41304.

[19] K. Dai, J. Mao, Z. Zhuo, Y. Feng, W. Mao, G. Ai, F. Pan, Y.-d. Chuang, G. Liu, W. Yang, *Nano Energy* **2020**, 74, 104831.

[20] Y. Zhang, M. Wu, J. Ma, G. Wei, Y. Ling, R. Zhang, Y. Huang, *ACS Cent. Sci.* **2020**, 6, 232.

[21] E. J. Kim, L. A. Ma, L. C. Duda, D. M. Pickup, A. V. Chadwick, R. Younesi, J. T. S. Irvine, A. R. Armstrong, *ACS Appl. Energy Materials* **2019**, 3, 184.

[22] Z. Lu, J. R. Dahn, *J. Electrochem. Soc.* **2001**, 148, A1225.

[23] R. J. Clément, J. Xu, D. S. Middlemiss, J. Alvarado, C. Ma, Y. S. Meng, C. P. Grey, *J. Mater. Chem. A* **2017**, 5, 4129.

[24] E. de la Llave, P. K. Nayak, E. Levi, T. R. Penki, S. Bublil, P. Hartmann, F.-F. Chesneau, M. Greenstein, L. F. Nazar, D. Aurbach, *J. Mater. Chem. A* **2017**, 5, 5858.

[25] E. de la Llave, E. Talaie, E. Levi, P. K. Nayak, M. Dixit, P. T. Rao, P. Hartmann, F. Chesneau, D. T. Major, M. Greenstein, D. Aurbach, L. F. Nazar, *Chem. Mater.* **2016**, 28, 9064.

[26] J. Xu, D. H. Lee, R. J. Clément, X. Yu, M. Leskes, A. J. Pell, G. Pintacuda, X.-Q. Yang, C. P. Grey, Y. S. Meng, *Chem. Mater.* **2014**, 26, 1260.

[27] D. Kim, M. Cho, K. Cho, *Adv. Mater.* **2017**, 29, 1701788.

[28] B. Xiao, X. Liu, M. Song, X. Yang, F. Omenya, S. Feng, V. Sprenkle, K. Amine, G. Xu, X. Li, D. Reed, *Nano Energy* **2021**, 89, 106371.

[29] J. H. Song, K. Wang, J. M. Zheng, M. H. Engelhard, B. W. Xiao, E. Y. Hu, Z. H. Zhu, C. M. Wang, M. L. Sui, Y. H. Lin, D. Reed, V. L. Sprenkle, P. F. Yan, X. L. Li, *ACS Energy Lett.* **2020**, 5, 1718.

[30] W. Yang, T. P. Devereaux, *J. Power Sources* **2018**, 389, 188.

[31] S. Roychoudhury, R. Qiao, Z. Zhuo, Q. Li, Y. Lyu, J. H. Kim, J. Liu, E. Lee, B. J. Polzin, J. Guo, S. Yan, Y. Hu, H. Li, D. Prendergast, W. Yang, *Energy Environ. Sci.* **2020**, 4, 246.

[32] W. E. Gent, I. I. Abate, W. Yang, L. F. Nazar, W. C. Chueh, *Joule* **2020**, 4, 1369.

[33] G. H. Lee, J. Wu, D. Kim, K. Cho, M. Cho, W. Yang, Y. M. Kang, *Angew. Chem. Int. Ed.* **2020**, 59, 8681.

[34] D. Eum, B. Kim, S. J. Kim, H. Park, J. Wu, S. P. Cho, G. Yoon, M. H. Lee, S. K. Jung, W. Yang, W. M. Seong, K. Ku, O. Tamwattana, S. K. Park, I. Hwang, K. Kang, *Nat. Mater.* **2020**, 19, 419.

[35] Z. Zhuo, C. D. Pemmaraju, J. Vinson, C. Jia, B. Moritz, I. Lee, S. Sallies, Q. Li, J. Wu, K. Dai, Y. D. Chuang, Z. Hussain, F. Pan, T. P. Devereaux, W. Yang, *J. Phys. Chem. Lett.* **2018**, 9, 6378.

[36] Z. Zhuo, Y. S. Liu, J. Guo, Y. D. Chuang, F. Pan, W. Yang, *J. Phys. Chem. Lett.* **2020**, 11, 2618.

[37] Z. Zhuo, K. Dai, R. Qiao, R. Wang, J. Wu, Y. Liu, J. Peng, L. Chen, Y.-d. Chuang, F. Pan, Z.-x. Shen, G. Liu, H. Li, T. P. Devereaux, W. Yang, *Joule* **2021**, 5, 975.

[38] E. Y. Hu, X. Q. Yu, R. Q. Lin, X. X. Bi, J. Lu, S. M. Bak, K. W. Nam, H. L. L. Xin, C. Jaye, D. A. Fischer, K. Amine, X. Q. Yang, *Nature Energy* **2018**, 3, 690.

[39] S. M. Kang, D. Kim, K. S. Lee, M. S. Kim, A. Jin, J. H. Park, C. Y. Ahn, T. Y. Jeon, Y. H. Jung, S. H. Yu, J. Mun, Y. E. Sung, *Adv. Sci.* **2020**, 7, 2001263.

[40] B. Xiao, H. Liu, N. Chen, M. N. Banis, H. Yu, J. Liang, Q. Sun, T. K. Sham, R. Li, M. Cai, G. A. Botton, X. Sun, *Angew. Chem. Int. Ed.* **2020**, 59, 14313.

[41] R. Qiao, Q. Li, Z. Zhuo, S. Sallis, O. Fuchs, M. Blum, L. Weinhardt, C. Heske, J. Pepper, M. Jones, A. Brown, A. Spucces, K. Chow, B. Smith, P. A. Glans, Y. Chen, S. Yan, F. Pan, L. F. Piper, J. Denlinger, J. Guo, Z. Hussain, Y. D. Chuang, W. Yang, *Rev. Sci. Instrum.* **2017**, 88, 033106.

[42] G. Kresse, J. Furthmuller, *Phys. Rev. B Condens. Matter.* **1996**, 54, 11169.

[43] J. P. Perdew, K. Burke, M. Ernzerhof, *Phys. Rev. Lett.* **1996**, 77, 3865.

[44] G. Hautier, S. P. Ong, A. Jain, C. J. Moore, G. Ceder, *Phys. Rev. B* **2012**, 85, 155208.

Entry for the Table of Contents

P2-type manganese-rich cathodes can have stabilized oxygen redox through doping Li/Mg to create unhybridized O 2p orbitals or introducing high covalency transition metals to induce a reductive coupling effect. This study on the model materials of P2-Na0.66Mn0.75Ni0.25O2 with and without Li doping reveals that the doped Li has complicated interactions with transition metals leading to an unusual oxygen redox suppression.

Biwei Xiao[†1], Xiang Liu[†2], Xi Chen[3], Gi-Hyeok Lee[4,5], Miao Song[6], Xin Yang[1], Fred Omenya[1], David M. Reed[1], Vincent Sprenkle[1], Yang Ren[7], Cheng-Jun Sun[7], Wanli Yang[4], Khalil Amine[2,8], Xin Li[3], Guiliang Xu[2*], Xiaolin Li[1*]*

Uncommon Behavior of Li Doping Suppresses Oxygen Redox in P2-type Manganese-Rich Sodium Cathodes